J Adv Ceram

Research Article

Phase evolution and broadband electromagnetic wave absorption mechanisms of electrospun polymer-derived SiC-based fibrous ceramic membranes

Gaoang Huang[1], Defang Zu[1], Xuewen Jiang[1], Mengru Li[1], Wei Li[1,✉], Limeng Song[1,2], Fan Zhang[1,3], Hailong Wang[1], Yu Chen[4], Yanqiu Zhu[5,6], Rui Zhang[1], Bingbing Fan[1,✉]

Cite this article: Huang G, Zu D, Jiang X, et al. *J Adv Ceram* 2026, **15**(8): 9221349. https://doi.org/10.26599/JAC.2026.9221349

ABSTRACT: Polymer-derived SiC-based ceramic fibrous membranes have attracted increasing attention as lightweight and thermally stable electromagnetic wave absorbers. However, simultaneously achieving strong attenuation capability and good impedance matching remains challenging due to the limited regulation of phase composition and dielectric behavior. In this work, multiphase SiC-based fibrous membranes were prepared by electrospinning combined with polycarbosilane (PCS)-derived ceramic conversion. The phase evolution, fiber morphology, dielectric response, and electromagnetic wave absorption performance were regulated by tuning the PCS content and pyrolysis temperatures. Advanced characterizations confirm the formation of a heterogeneous β-SiC/SiO_xC_y/carbon multiphase structure with good flexibility, which provides abundant polarization centers, moderate conductive pathways, and multiple reflection sites, thereby enabling balanced impedance matching and dielectric loss. Consequently, the sample with a PCS content of 1.4 g pyrolyzed at 1400 °C achieves a minimum reflection loss (RL_{min}) of −27.12 dB at a matching thickness of 2.2 mm and a maximum effective absorption bandwidth (EAB) of 8.22 GHz at 2.7 mm, covering 9.78–18 GHz. Radar cross-section (RCS) simulation further verifies the electromagnetic scattering suppression capability of the optimized fibrous ceramic coating. Therefore, this study provides a useful strategy for tailoring the phase composition and dielectric behavior in polymer-derived SiC-based fibrous membranes for broadband electromagnetic wave absorption.

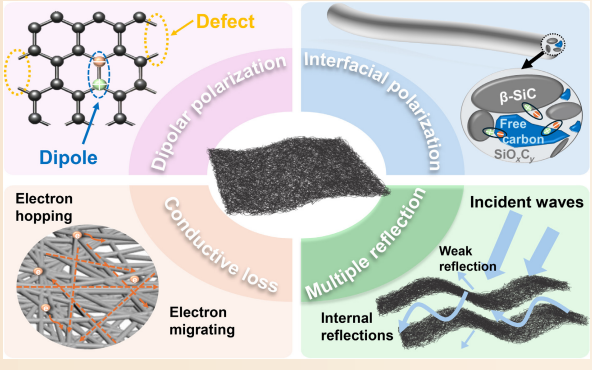

KEYWORDS: SiC-based fibrous membranes; phase evolution; polycarbosilane (PCS); polymer-derived ceramics (PDCs); electromagnetic wave absorption

1 Introduction

With the rapid development of high-frequency electronic devices and wireless communication technologies, electromagnetic pollution has become an increasingly serious concern [1–4]. This trend has generated a growing demand for high-performance electromagnetic wave (EMW)-absorbing materials with lightweight characteristics, small thickness, wide effective absorption bandwidth, and strong absorption intensity [5,6]. Conventional polymer-based absorbers often suffer from thermal degradation and structural instability at elevated temperatures, whereas metal-based absorbers are limited by their high density, poor corrosion resistance, and performance deterioration arising from surface oxidation [7–9]. Among the various high-temperature microwave absorbing materials, silicon carbide (SiC) ceramics are widely considered one of the most promising candidates for harsh-environment applications owing to their low density, excellent chemical and thermal stability, superior mechanical strength, and intrinsic semiconducting characteristics [10–13].

[1] School of Materials Science and Engineering, Zhengzhou University, Zhengzhou 450001, China. [2] Henan Key Laboratory of Aeronautical Materials and Application Technology, Henan International Joint Laboratory of Aeronautical Function Materials and Advanced Processing Technology, School of Material Science and Engineering, Zhengzhou University of Aeronautics, Zhengzhou 450015, China. [3] Institute of Advanced Ceramics, Henan Academy of Science, Zhengzhou 450046, China. [4] Department of Materials, Design and Manufacturing Engineering, School of Engineering, University of Liverpool, Liverpool L69 3GH, UK. [5] State Key Laboratory of Featured Metal Materials and Life-cycle Safety for Composite Structures, MOE Key Laboratory of New Processing Technology for Nonferrous Metals and Materials, and School of Resources, Environment and Materials, Guangxi University, Nanning 530004, China. [6] Department of Engineering, Faculty of Environment, Science and Economy, University of Exeter, Exeter EX4 4QF, UK.

✉ Corresponding authors. E-mail: W. Li, liw@zzu.edu.cn; B. Fan, fanbingbing@zzu.edu.cn

Received: May 22, 2026; Revised: July 2, 2026; Accepted: July 9, 2026

However, the EMW absorption performance of stoichiometric SiC is generally constrained by its relatively low dielectric loss capability and inadequate impedance matching, leading to limited attenuation efficiency and narrow effective absorption bandwidths [14–19]. To address these limitations, structural engineering and compositional modulation have been widely explored as effective approaches [20–23]. In particular, the incorporation of heterogeneous interfaces and the regulation of secondary phases, including silicon oxycarbide (SiO_xC_y) and amorphous carbon, can markedly improve EMW attenuation by promoting interfacial polarization and multiple dielectric loss mechanisms [24,25]. Among the available fabrication strategies, the polymer-derived ceramic (PDC) route offers a unique advantage by allowing for the precise control of the ceramic's chemical composition and microstructure at the molecular level through the design of preceramic polymers [26–29]. Feng *et al.* [30] prepared SiOC ceramics via a combination of digital light processing (DLP) three-dimensional (3D) printing and the PDC route. The *in situ* generated free carbon and β-SiC nanocrystals effectively enhanced interfacial and dipolar polarization, resulting in a minimum reflection loss (RL_{min}) of −23.5 dB and an effective absorption bandwidth (EAB) of 4.9 GHz at a thickness of 1.58 mm. Duan *et al.* [31] developed nano-SiC-modified SiOC ceramics (n-SiC/SiOC) by pyrolyzing polysiloxane containing 30 nm SiC nanoparticles. The sample annealed at 1400 °C achieved an RL_{min} of −61 dB at 8.6 GHz and an EAB of 3.5 GHz in the X-band, demonstrating significantly improved microwave absorption performance compared with pure SiOC ceramics.

When coupled with electrospinning technology, the PDC route enables the scalable production of continuous micro/nanofibers. These fibrous structures not only inherit the intrinsic merits of SiC ceramics but also provide ultralow density and high aspect ratios [32–34]. Furthermore, the 3D interconnected fibrous networks can extend the propagation path of EM waves through multiple reflections and scattering, thereby significantly boosting the absorption efficiency [33,35]. Chen *et al.* [36] fabricated lightweight SiBCN nanofibers by electrospinning and the PDC route, demonstrating that the synergistic effect between *in situ* formed β-SiC and free carbon significantly enhanced dielectric polarization. The optimized sample, annealed at 1600 °C, achieved an RL_{min} of −56.9 dB and an EAB of 3.45 GHz in the X-band.

Despite these advances, several fundamental issues concerning polymer-derived SiC-based fibrous ceramic absorbers remain inadequately elucidated. Specifically, the synergistic evolution of β-SiC crystallization, amorphous SiO_xC_y phase formation, and free-carbon structural ordering during pyrolysis has not been systematically correlated with the resulting dielectric response. Moreover, the respective contributions of heterogeneous interfacial structures and carbon-induced conductive pathways to impedance matching and electromagnetic attenuation mechanisms remain insufficiently clarified. In addition, current studies predominantly emphasize the optimization of final microwave absorption performance, whereas the intrinsic structure–dielectric property–absorption relationship governed by precursor composition and pyrolysis conditions has yet to be comprehensively established. Therefore, elucidating the correlation between phase evolution and electromagnetic wave attenuation behavior in PDC-derived SiC ceramics is of critical importance for the rational design and optimization of advanced ceramic absorbers with broadband absorption in the X and Ku bands.

In this study, electrospinning and PDC route were combined to prepare multiphase SiC-based fibrous membranes. By regulating the polycarbosilane (PCS) content and pyrolysis temperatures, the relative formation of β-SiC, amorphous SiO_xC_y, and free carbon was tailored. The dielectric parameters, impedance matching behavior, attenuation capability, and radar scattering suppression of the obtained membranes were systematically investigated.

2 Experimental methods

2.1 Materials

Polycarbosilane (PCS) precursor was provided by the Institute of Chemistry, Chinese Academy of Sciences; tetrahydrofuran (THF) was purchased from Xilong Scientific Co., Ltd.; polyvinylpyrrolidone (PVP) was produced by Shanghai Macklin Biochemical Co., Ltd.; N,N-dimethylformamide (DMF) was obtained from Beijing InnoChem Science & Technology Co., Ltd.

2.2 Fabrication of SiC-based fiber membrane

To evaluate the effect of PCS content on the microstructures and properties of the samples, three precursor solutions with different PCS concentrations were designed, as summarized in Table 1. A schematic illustration of the SiC-based fibrous membrane preparation process is presented in Fig. 1(a). Specifically, PCS and PVP were dissolved in a mixed solvent of THF and DMF, followed by magnetic stirring at ambient temperature for 12 h to form homogeneous spinning solutions. The prepared solutions were subsequently transferred into 5 mL plastic syringes equipped with a 20 G stainless-steel needle for electrospinning. A positive voltage of 9 kV was applied between the needle and a rotating aluminum foil collector with a tip-to-collector distance of 10 cm. Electrospinning was conducted at a flow rate of 1.5 mL/h, and the as-spun precursor fiber membrane was continuously collected on the rotating collector. To stabilize the fiber morphology and prevent interfiber fusion during subsequent pyrolysis, the as-spun precursor fiber mats were subjected to a crosslinking curing treatment at 200 °C for 2 h in a drying oven. During the oxidative curing process, oxygen from air is incorporated into the PCS molecular chains through the formation of Si–O–Si and Si–O–C cross-linked structures. Such oxygen-containing networks effectively suppress fiber melting during subsequent pyrolysis and serve as the precursor of the amorphous SiO_xC_y phase formed after ceramic conversion.

Subsequently, the cured fiber membrane was thermally annealed in a tube furnace under an argon atmosphere. The pyrolysis temperature was first increased from room temperature to 1100 °C at a heating rate of 3 °C/min, followed by further heating to 1300–1500 °C for 2 h at a heating rate of 2 °C/min and finally cooling to room temperature. The samples obtained at different temperatures (1300, 1400, and 1500 °C) were denoted PCS-1.2-1300, PCS-1.2-1400, PCS-1.2-1500, PCS-1.4-1300, PCS-1.4-1400, PCS-1.4-1500, PCS-1.6-1300, PCS-1.6-1400, and PCS-1.6-1500, respectively.

2.3 Characterization of SiC-based fibrous membranes

The phase composition of the obtained samples was analyzed by an X-ray diffractometer (XRD; Empyrean X, PANalytical,

Table 1 Precursor solution parameters for the SiC-based fibrous membranes

Sample name	PCS (g)	THF (mL)	PVP (g)	DMF (mL)
PCS-1.2	1.2	9.0	0.5	4
PCS-1.4	1.4	10.5	0.5	4
PCS-1.6	1.6	12.0	0.5	4

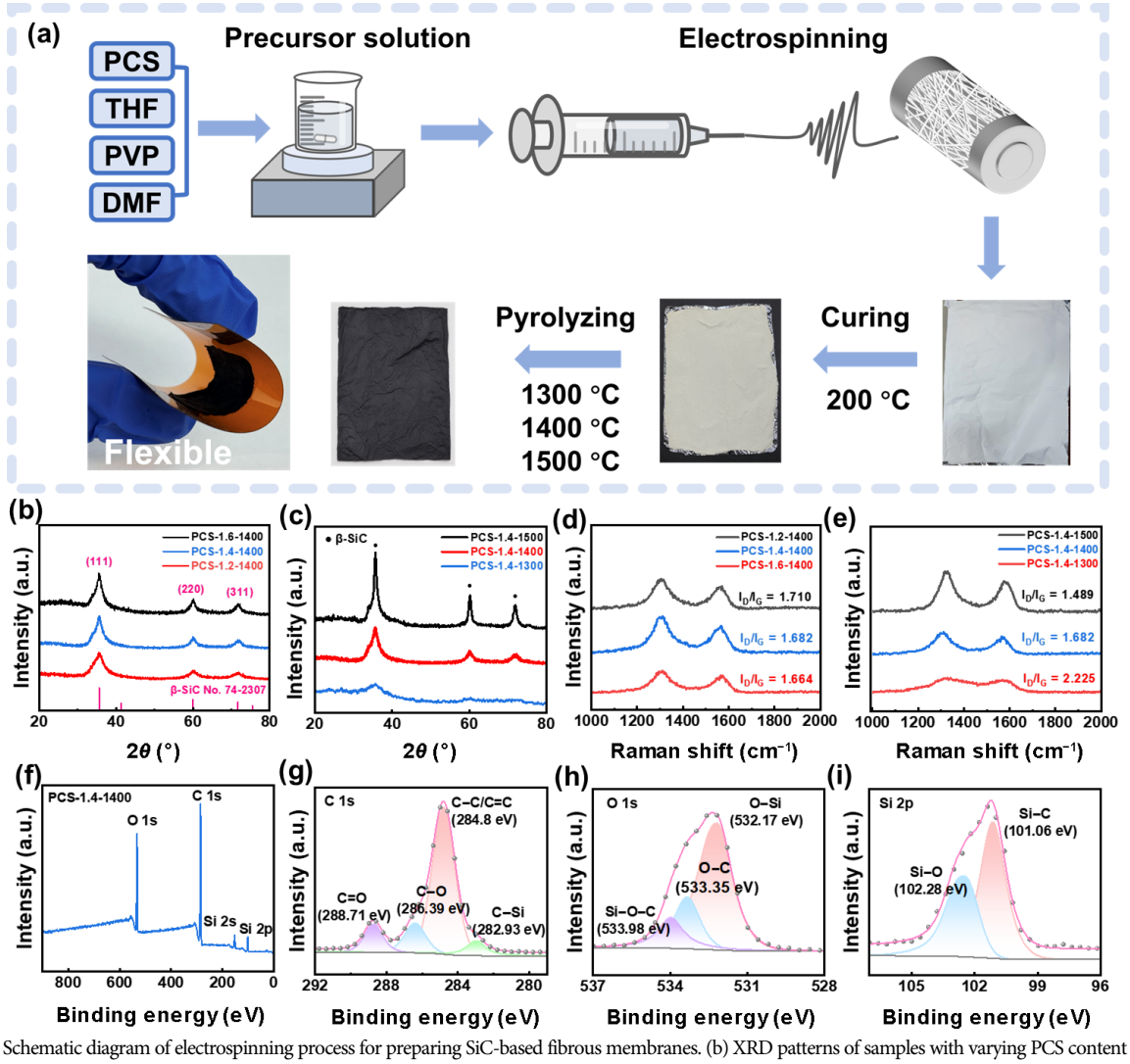

Fig. 1 (a) Schematic diagram of electrospinning process for preparing SiC-based fibrous membranes. (b) XRD patterns of samples with varying PCS content pyrolyzed at 1400 °C. (c) XRD patterns of PCS-1.4 samples pyrolyzed at different temperatures. Raman spectra of different samples: (d) samples with varying PCS content pyrolyzed at 1400 °C and (e) PCS-1.4 sample pyrolyzed at different temperatures. (f) XPS full spectrum of SiC-based fibrous membranes, (g) C 1s refined spectrum, (h) O 1s refined spectrum, and (i) Si 2p refined spectrum.

Netherlands) with Cu Kα radiation. The morphology of the samples was characterized by a field-emission scanning electron microscope (SEM; JSM-IT800, JEOL, Japan). The internal microstructure of the samples was analyzed using a high-resolution transmission electron microscope (HRTEM; JEM-F200, JEOL, Japan), and the elemental distribution was concurrently examined using energy-dispersive X-ray spectroscopy (EDS). The fiber diameter distribution was statistically analyzed from SEM images using ImageJ software. For each sample, at least 100 fibers were randomly measured from three different SEM images, and the average fiber diameter was statistically calculated and expressed as the mean±standard deviation. The chemical valence states of the resulting samples were characterized by an X-ray photoelectron spectrometer (XPS; Thermo Scientific K-Alpha, USA). Raman spectra of the SiC-based fiber membranes were recorded using a laser Raman spectrometer (LabRAM HR Evolution, HORIBA FRANCE SAS, France) at excitation wavelengths of 532 nm. The SiC-based fibrous membranes were cut into small pieces and uniformly mixed with paraffin wax at a mass ratio of 1 : 10 and then pressed into toroidal samples with an outer diameter of 7 mm, an inner diameter of 3.04 mm, and a thickness of approximately 2 mm. The electromagnetic parameters of the resulting SiC-based fibrous membranes/paraffin composites were measured using a vector network analyzer (VNA; E5080D, Keysight, USA) over the frequency range of 2–18 GHz via the APC7 coaxial transmission line method. The same filler loading was adopted for all samples to ensure the reliability and comparability of the measured results.

3 Results and discussion

3.1 Phase evolution and microstructural characteristics of polymer-derived SiC-based fibrous membranes

To confirm the phase composition, XRD characterization was performed, as shown in Fig. 1(b). Distinct diffraction peaks located at $2\theta \approx 35.6°$, 60.0°, and 71.8° are observed for all samples, which can be indexed to the (111), (220), and (311) crystal planes of β-SiC (JCPDS No. 74-2307), respectively. Notably, the diffraction peaks remain relatively broad, suggesting the coexistence of nanocrystalline β-SiC domains and amorphous phases within the ceramic matrix. In addition, the diffraction intensity gradually increases with increasing PCS content, indicating enhanced nucleation and growth of β-SiC crystallites.

This result suggests that a higher PCS content promotes a more sufficient precursor-to-ceramic conversion and consequently improves the crystallinity of the resulting SiC ceramics. Figure 1(c) further shows the XRD patterns of PCS-1.4 samples pyrolyzed at different temperatures (1300–1500 °C). (The XRD patterns of PCS-1.2 and PCS-1.6 pyrolyzed at different temperatures are presented in Figs. S1(a) and S1(b) in the Electronic Supplementary Material (ESM)). At 1300 °C, the XRD patterns of samples with different PCS contents all show low-intensity and broad diffraction peaks, indicating that the samples are at the incipient nucleation stage with low crystallinity. When the temperature is raised to 1400 and 1500 °C, the characteristic diffraction peaks of β-SiC emerge and progressively intensify, accompanied by peak narrowing, reflecting an improvement in crystalline ordering and crystallinity [37]. To further quantify the crystallization behavior of β-SiC during pyrolysis, the full width at half maximum (FWHM) of the characteristic diffraction peak located at approximately 35.6° was extracted from the XRD patterns. The average crystallite size of β-SiC was estimated from the FWHM of the (111) diffraction peak based on the Scherrer equation (Eq. (1)):

$$D = \frac{k\lambda}{\beta\cos\theta} \tag{1}$$

where D denotes the average crystallite size; k represents the shape factor; λ is the X-ray wavelength of Cu Kα radiation; β signifies the FWHM in radians; θ is the Bragg diffraction angle. The calculated results are summarized in Table S1 in the ESM. With increasing pyrolysis temperature from 1300 to 1500 °C, the FWHM values of the β-SiC diffraction peaks gradually decrease, while the estimated crystallite size increases, indicating the progressive crystallization and grain growth of β-SiC. Meanwhile, the diffraction peaks remain relatively broadened even at 1500 °C, suggesting that nanocrystalline β-SiC is still embedded in an amorphous ceramic matrix [38,39]. Notably, the weak diffraction peak located at approximately 34° in the PCS-1.4-1500 sample can be assigned to stacking faults in β-SiC. The formation of stacking faults reflects the generation of crystallographic defects during high-temperature structural rearrangement [38]. These defects may act as additional dipolar polarization centers under an alternating electromagnetic field, contributing to dielectric relaxation. However, excessive crystallization and defect evolution at 1500 °C may also disturb the balance between dielectric loss and impedance matching, which is unfavorable for broadband electromagnetic wave absorption.

Raman spectroscopy was also conducted to characterize the structure of the carbon phase. As shown in Figs. 1(d) and 1(e), two typical peaks at approximately 1310 and 1580 cm^{-1} assigned to the D and G peaks of carbon manifest a certain amount of excess carbon in the SiC matrix [40]. The intensity ratio of the D band to G band (I_D/I_G) is commonly used to evaluate the degree of structural disorder in carbon materials. As shown in Fig. 1(d), the I_D/I_G values are 1.710 for PCS-1.2-1400, 1.682 for PCS-1.4-1400, and 1.664 for PCS-1.6-1400, suggesting a reduction in defect density and an improvement in the structural ordering of the carbon phase. This evolution can be attributed to the enhanced formation of Si–C networks at higher PCS contents, which constrains the distribution of free carbon and suppresses the generation of highly disordered carbon species. For PCS-1.4-1400, such moderated carbon ordering is beneficial for establishing stable conductive pathways while avoiding excessive conductivity. In contrast, the effect of heat-treatment temperature on the carbon structure is more notable. As presented in Fig. 1(e), higher pyrolysis temperatures promote the structural ordering of carbon, resulting in an increased degree of graphitization accompanied by a gradual decrease in the I_D/I_G ratio.

The chemical composition and bonding states of the obtained SiC-based fibrous membranes were characterized by XPS with the corresponding spectra presented in Figs. 1(f)–1(i). Clear signals corresponding to C 1s, O 1s, and Si 2p are observed, suggesting the coexistence of carbon, silicon, and oxygen on the sample surface. To further clarify the chemical bonding composition, the relative peak areas obtained from XPS deconvolution are summarized in Table S2 in the ESM. In the C 1s spectrum (Fig. 1(g)), four characteristic peaks at approximately 282.93, 284.80, 286.39, and 288.71 eV are assigned to C–Si, C–C/C=C, C–O, and C=O bonds, respectively. The dominant C–C/C=C component (67.61%) confirms the presence of abundant disordered free carbon, while the detected C–Si bonds confirm that a portion of carbon is incorporated into the SiC lattice. The O 1s spectrum (Fig. 1(h)) shows three components assigned to O–Si, O–C, and Si–O–C bonds. In the Si 2p spectrum (Fig. 1(i)), the peaks at approximately 101.06 and 102.28 eV correspond to Si–C and Si–O bonds, respectively. Together with the detectable Si–O–C bonds (15.4%), these results confirm the coexistence of crystalline SiC and amorphous SiO_xC_y transitional phases [41]. The formation of such multiphase structures may be attributed to oxidative curing and subsequent pyrolysis processes. During oxidative curing, oxygen is introduced into the PCS precursor through the formation of Si–O–Si and Si–O–C crosslinked structures. After pyrolysis, the precursor is transformed into β-SiC, whereas the residual oxygen-containing species evolve into amorphous SiO_xC_y phases. Meanwhile, excess carbon atoms that are not fully bonded with Si remain as disordered free carbon. Consequently, a multiphase ceramic composed of β-SiC, free carbon, and amorphous SiO_xC_y is formed, generating abundant heterogeneous interfaces and polarization centers favorable for electromagnetic wave attenuation.

Quantitative elemental analysis based on EDS was carried out to reveal the compositional evolution of multiphase fibrous ceramics regulated by precursor dosage and pyrolysis temperature. As shown in Fig. S2(a) in the ESM, increasing the PCS content results in a gradual increase in the carbon and oxygen content, accompanied by a decrease in the silicon content, which demonstrates that a higher precursor dosage facilitates the precipitation of free carbon domains and retains more amorphous SiO_xC_y within the ceramic matrix. In contrast, increasing the pyrolysis temperature significantly decreases the oxygen content while increasing the silicon content (Fig. S2(b) in the ESM), which is attributed to the progressive carbothermal conversion of the amorphous SiO_xC_y into crystalline β-SiC.

Figures S3(a)–S3(c) in the ESM present SEM images of the as-spun fibrous membranes prepared with different PCS contents and the corresponding fiber diameter distributions. All samples form continuous and bead-free fibrous networks with random orientation, indicating good spinnability and stability of the precursor solutions. As the PCS content increases, the average fiber diameter gradually increases from approximately 0.740 to 1.018 μm. This behavior is mainly attributed to the increased viscosity and enhanced molecular chain entanglement of the spinning solution induced by higher PCS loading, which weakens the electrostatic stretching effect during electrospinning and consequently results in thicker fibers. After curing at 200 °C (Figs. S3(d)–S3(f) in the ESM), the average fiber diameter slightly decreases to 0.698–1.005 μm, indicating mild shrinkage and densification during the curing process. It is mainly associated

with residual solvent evaporation, oxidative crosslinking of PCS chains, and molecular chain rearrangement of PVP. The overall fibrous architectures are well preserved without noticeable fiber breakage or fusion, demonstrating that the curing process does not compromise the structural integrity of the membranes. Compared with the as-spun counterparts, the cured fibers display more rigid and well-defined morphologies, which is mainly associated with the crosslinking reactions of PCS during thermal curing. The effect of PCS content on the microstructure of fibers after pyrolysis at 1400 °C is further characterized by SEM (Figs. 2(a)–2(c)). With increasing PCS content, the average fiber diameter increases from 0.373 to 0.625 μm. Additionally, high-temperature pyrolysis induces the carbothermal conversion of amorphous SiO_xC_y into crystalline β-SiC, accompanied by the evolution of gaseous CO and SiO (Reactions (2)–(4)). The decomposition of organic species and the progressive ceramization process result in noticeable fiber shrinkage, while the escape of gaseous products contributes to the formation of rough fiber surfaces [37,42].

$$SiO_xC_y \rightarrow SiC\,(s) + C\,(s) + CO\,(g) + SiO(g) \quad (2)$$

$$SiO(g) + 2C(s) \rightarrow CO(g) + SiC(s) \quad (3)$$

$$SiO\,(g) + 3CO\,(g) \rightarrow 2CO_2\,(g) + SiC(s) \quad (4)$$

The escaping gases generate internal micropores, nanoscale defects, and abundant heterogeneous interfaces within the fibers, which serve as effective polarization centers and promote polarization relaxation. Meanwhile, the bamboo-like segmented morphology, originating from solvent evaporation and phase separation during fiber formation, together with micropores and heterointerfaces, provides abundant scattering centers and tortuous propagation paths. This enhances multiple scattering and reflection, extending the EM wave transmission distance and improving the attenuation efficiency. Furthermore, the segmented structure disrupts excessive conductive pathways, maintaining moderate permittivity and favorable impedance matching. The synergy of polarization losses, multiple scattering, and optimized impedance matching accounts for its superior absorption performance. Benefiting from the three-dimensionally crosslinked fiber network structure, the SiC fibrous membrane exhibits outstanding flexibility (Fig. 1).

In addition, the microstructure and phase composition of PCS-1.4-1400 were further characterized by HRTEM, selected-area electron diffraction (SAED), and elemental mapping analyses, as presented in Figs. 2(g)–2(j). The HRTEM images in Figs. 2(d) and 2(f) exhibit clear lattice fringes with an interplanar spacing of approximately 0.25 nm, which can be assigned to the (111) crystal plane of β-SiC, confirming the successful polymer-to-ceramic conversion of PCS and the generation of nanocrystalline β-SiC during pyrolysis. Some amorphous regions can also be observed in the HRTEM images. Their formation is associated with residual oxygen retained during pyrolysis, Si–O–Si network generated during oxidative curing, incomplete conversion of Si–O–C species, carbonization of PVP, and decomposition of PCS side chains. Combined with the XRD, Raman, and XPS analyses, these amorphous regions are identified as SiO_xC_y and amorphous

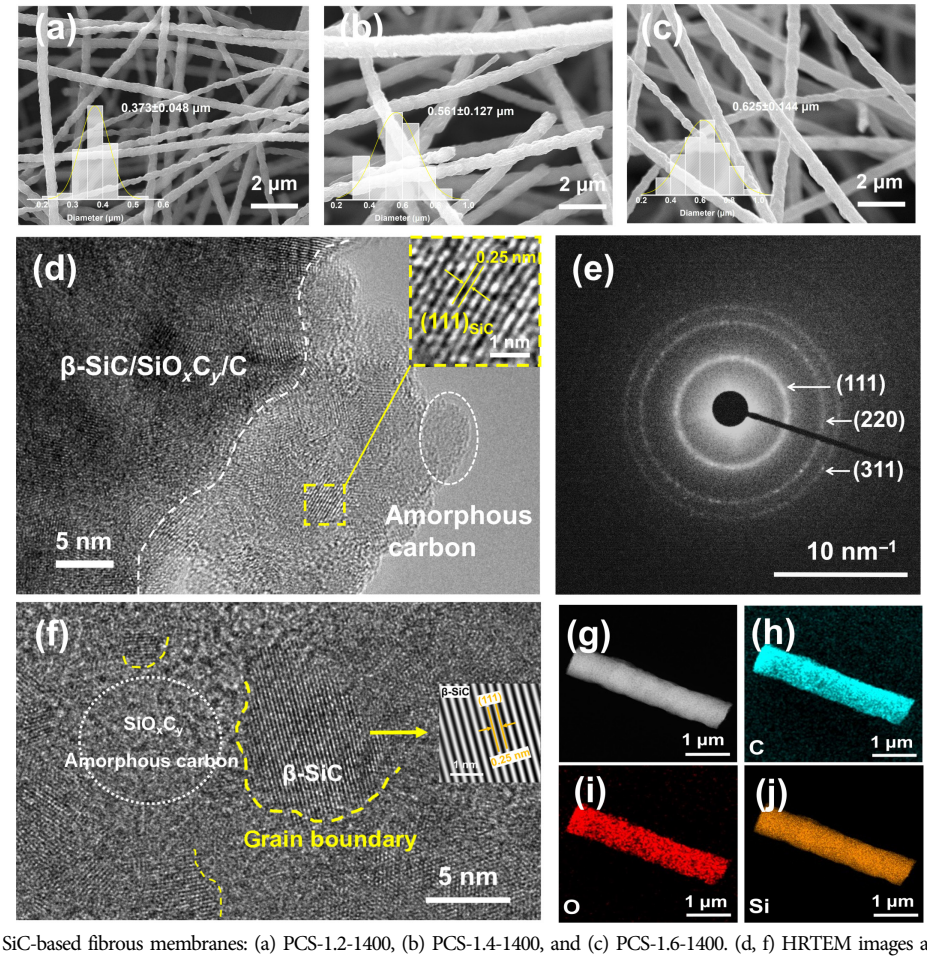

Fig. 2 SEM images of SiC-based fibrous membranes: (a) PCS-1.2-1400, (b) PCS-1.4-1400, and (c) PCS-1.6-1400. (d, f) HRTEM images and (e) SAED patterns of PCS-1.4-1400. (g–j) EDS mapping images of PCS-1.4-1400.

清華大学出版社 Tsinghua University Press | SciOpen

carbon phases. Meanwhile, abundant grain boundaries and heterogeneous interfaces between β-SiC nanocrystals and SiO_xC_y/amorphous carbon regions are observed in Fig. 2(f). Furthermore, the SAED pattern (Fig. 2(e)) exhibits distinct diffraction rings indexed to the (111), (220), and (311) planes of β-SiC. The ring-like diffraction rather than discrete spots suggests randomly oriented nanocrystals, which further indicates the polycrystalline nature of the ceramic phase with nanoscale grain size.

Additionally, elemental mapping results (Figs. 2(g)–2(j)) demonstrate that C, Si, and O are all uniformly distributed throughout the fibrous structure. The relatively high oxygen content observed in our samples should not be regarded as detrimental oxygen impurities but rather as an intrinsic structural feature of the SiO_xC_y ceramic matrix. This uniform component distribution is conducive to forming a homogeneous microstructure, thereby avoiding localized performance variations. Together with the coexisting nanocrystalline β-SiC and disordered carbon, these features form abundant grain boundaries and heterogeneous interfaces that enhance interfacial and dipolar polarization losses, thereby improving the overall EMW absorption performance [43].

3.2 EM parameter analysis and EMW absorption properties

The real part (ε') and imaginary part (ε'') of the complex permittivity, together with the dielectric loss tangent ($\tan\delta_\varepsilon$) of the samples prepared with different PCS contents are presented in Fig. 3. The real part of the permittivity (ε') reflects the polarization capability of the material under an alternating electromagnetic field, whereas the imaginary part (ε'') represents the capability to dissipate electromagnetic energy. The dielectric loss tangent ($\tan\delta_\varepsilon = \varepsilon''/\varepsilon'$) is commonly used to evaluate the efficiency of electromagnetic energy attenuation and conversion within the material [44]. All samples exhibit a decrease in ε' with increasing frequency, which is a typical frequency dispersion behavior (Fig. 3(a)). This phenomenon is attributed to the lag of polarization processes relative to the alternating electromagnetic field at higher frequencies [45]. The resonance peaks in the mid-to-high frequency range are attributed to carrier concentration and electron transport variations arising from the multiphase dielectric composition [46].

To quantitatively distinguish the respective contributions of conductive loss and polarization loss, the electromagnetic parameters were fitted using the least squares method based on the modified Debye relaxation model [29]. As shown in Fig. 3(f), polarization loss is identified as the dominant dielectric dissipation mechanism, accounting for approximately 60%–70% of the total dielectric loss. The enhanced polarization relaxation originates from abundant heterogeneous interfaces among β-SiC, amorphous SiO_xC_y, and free carbon, as well as defect sites generated during carbothermal conversion. All prepared samples are nonmagnetic materials free of ferromagnetic phases. The measured relative complex permeability shows that μ' remains at approximately 1.0 and that μ'' fluctuates near 0 within the whole 2–18 GHz frequency band (Fig. S4 in the ESM), yielding a negligible magnetic loss tangent $\tan\delta_\mu$. Therefore, the relative permeability can be simplified as $\mu_r \approx 1$, and magnetic loss can be fully excluded from the energy dissipation mechanism.

To further analyze the dielectric relaxation behavior and polarization mechanisms, Cole–Cole plots (ε'' versus ε') were constructed based on the Debye relaxation theory (Eq. (5)) [47]:

$$\left(\varepsilon' - \frac{\varepsilon_s + \varepsilon_\infty}{2}\right)^2 + (\varepsilon'')^2 = \left(\frac{\varepsilon_s + \varepsilon_\infty}{2}\right)^2 \tag{5}$$

where ε_s and ε_∞ are the static permittivity and high-frequency permittivity, respectively. In principle, each semicircle corresponds to one relaxation process [48]. As shown in Figs. S5(a)–S5(c) in the ESM, PCS-1.4-1400 and PCS-1.6-1400 exhibit more distorted semicircles than PCS-1.2-1400, implying enhanced dipolar polarization originating from structural defects and heterogeneous bonding configurations. The attenuation constant (α) was calculated according to Eq. (6) to evaluate the intrinsic electromagnetic wave dissipation capability of the samples [49]:

$$\alpha = \frac{\sqrt{2}}{c}\pi f \times \sqrt{(\mu''\varepsilon'' - \mu'\varepsilon') + \sqrt{(\mu''\varepsilon'' - \mu'\varepsilon')^2 + (\mu'\varepsilon'' - \mu''\varepsilon')^2}} \tag{6}$$

where f is the frequency; c signifies the speed of light; ε' and ε'' represent the real and imaginary parts of the complex permittivity; and μ' and μ'' are the real and imaginary parts of the complex permeability, respectively. As shown in Fig. S7(a) in the ESM, PCS-1.6-1400 exhibits the highest attenuation constant (α), followed by PCS-1.2-1400 and PCS-1.4-1400.

The electromagnetic wave absorption performance was evaluated using two representative parameters, namely, the RL_{min} and the EAB. The EAB is defined as the frequency range in which the RL values are lower than −10 dB, corresponding to more than 90% attenuation of incident electromagnetic waves. The RL values are calculated according to transmission line theory (Eqs. (7) and (8)) [50,51]:

$$\mathrm{RL\,(dB)} = 20\log\left|\frac{Z_{in} - Z_0}{Z_{in} + Z_0}\right| \tag{7}$$

$$Z_{in} = Z_0\sqrt{\frac{\mu_r}{\varepsilon_r}}\tanh\left(j\frac{2\pi fd}{c}\sqrt{\mu_r\varepsilon_r}\right) \tag{8}$$

where Z_{in} and Z_0 represent the impedance of the material and free space, respectively; c signifies the electromagnetic wave propagation speed in a vacuum; d is the thickness of the absorbing materials; ε_r and μ_r are the complex permittivity and complex permeability, respectively. As the value of impedance matching ($Z = Z_{in}/Z_0$) falls within 0.8–1.2, a larger fraction of electromagnetic waves can penetrate into the material rather than being reflected at the surface [6,52]. For PCS-1.2-1400 (Figs. 3(g) and 3(j)), an RL_{min} of approximately −23.84 dB is achieved at a thickness of approximately 2.2 mm, with an effective absorption bandwidth of approximately 7.45 GHz. This indicates a certain absorption capability, although the frequency coverage remains limited. In the case of PCS-1.6-1400 (Figs. 3(i) and 3(l)), the RL_{min} reaches approximately −17.92 dB at a thickness of approximately 2.0 mm, with a bandwidth of approximately 7.82 GHz. In contrast, PCS-1.4-1400 (Figs. 3(h) and 3(k)) exhibits the best comprehensive microwave absorption performance, achieving the lowest RL_{min} of −27.12 dB at a relatively thin thickness of approximately 2.2 mm, with a significantly broadened EAB of 9.78–18 GHz, corresponding to a bandwidth of 8.22 GHz.

However, the absorption performance cannot be determined solely by the dielectric loss or attenuation constant. Due to its excessively high dielectric constant, PCS-1.6-1400 exhibits poor impedance matching with a normalized input impedance deviating from unity over most frequency-thickness regions,

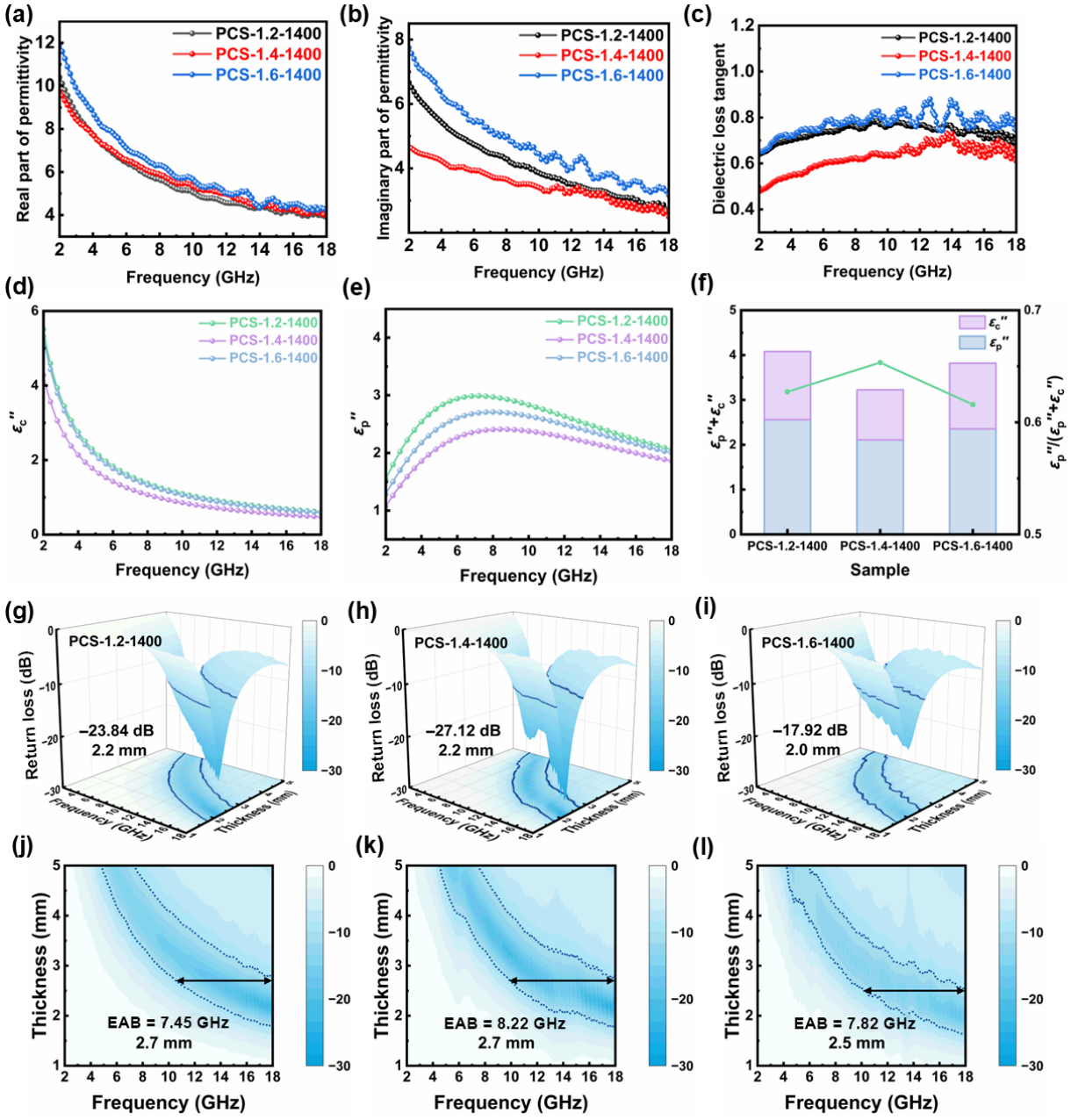

Fig. 3 (a) ε', (b) ε'', (c) $\tan\delta_\varepsilon$ of PCS-1.2-1400, PCS-1.4-1400, PCS-1.6-1400. Dielectric loss fitting results of samples with different PCS mass ratios: (d) frequency-dependent polarization loss, (e) frequency-dependent conductive loss, and (f) stacked column diagram of average loss magnitude and relative contribution ratio of polarization loss. EMW absorption properties for SiC-based fibrous membranes: (g–i) 3D and (j–l) two-dimensional (2D) plots of reflection loss (RL) for PCS-1.2-1400, PCS-1.4-1400, and PCS-1.6-1400, respectively.

causing increased surface reflection (Fig. S8 in the ESM). For PCS-1.2-1400, the relatively low crystallinity of SiC and the low graphitization degree of the carbon phase hinder effective charge transport and polarization relaxation, thereby limiting the overall dielectric loss capability. Consequently, the overall polarization loss remains weak, thereby restricting both the absorption intensity and bandwidth. A broad region with $|Z_{in}/Z_0|$ approaching 1 is obtained in the PCS-1.4-1400 sample, which overlaps well with the strong RL region, confirming that the optimized microwave absorption originates from the synergistic balance between efficient wave penetration and dielectric attenuation. Based on its favorable impedance matching performance and the maximum effective absorption bandwidth, the sample with a PCS content of 1.4 g was selected for further investigation of the effect of pyrolysis temperature on microwave absorption properties.

The influence of pyrolysis temperature on the microwave absorption properties of the PCS-1.4 sample is investigated, as shown in Figs. 4(a)–4(c). With increasing temperature, ε' and ε'' exhibit similar frequency-dependent decreasing trends. Among the three samples, PCS-1.4-1500 exhibits the highest ε'' and $\tan\delta_\varepsilon$ values over most of the measured frequency range, suggesting the strongest dielectric dissipation capability. This enhancement can be attributed to the increased graphitization degree and improved conductive pathways formed at elevated pyrolysis temperatures, which intensify conductive loss. In contrast, PCS-1.4-1300 shows relatively lower dielectric parameters due to insufficient crystallization of β-SiC and limited conductive carbon network

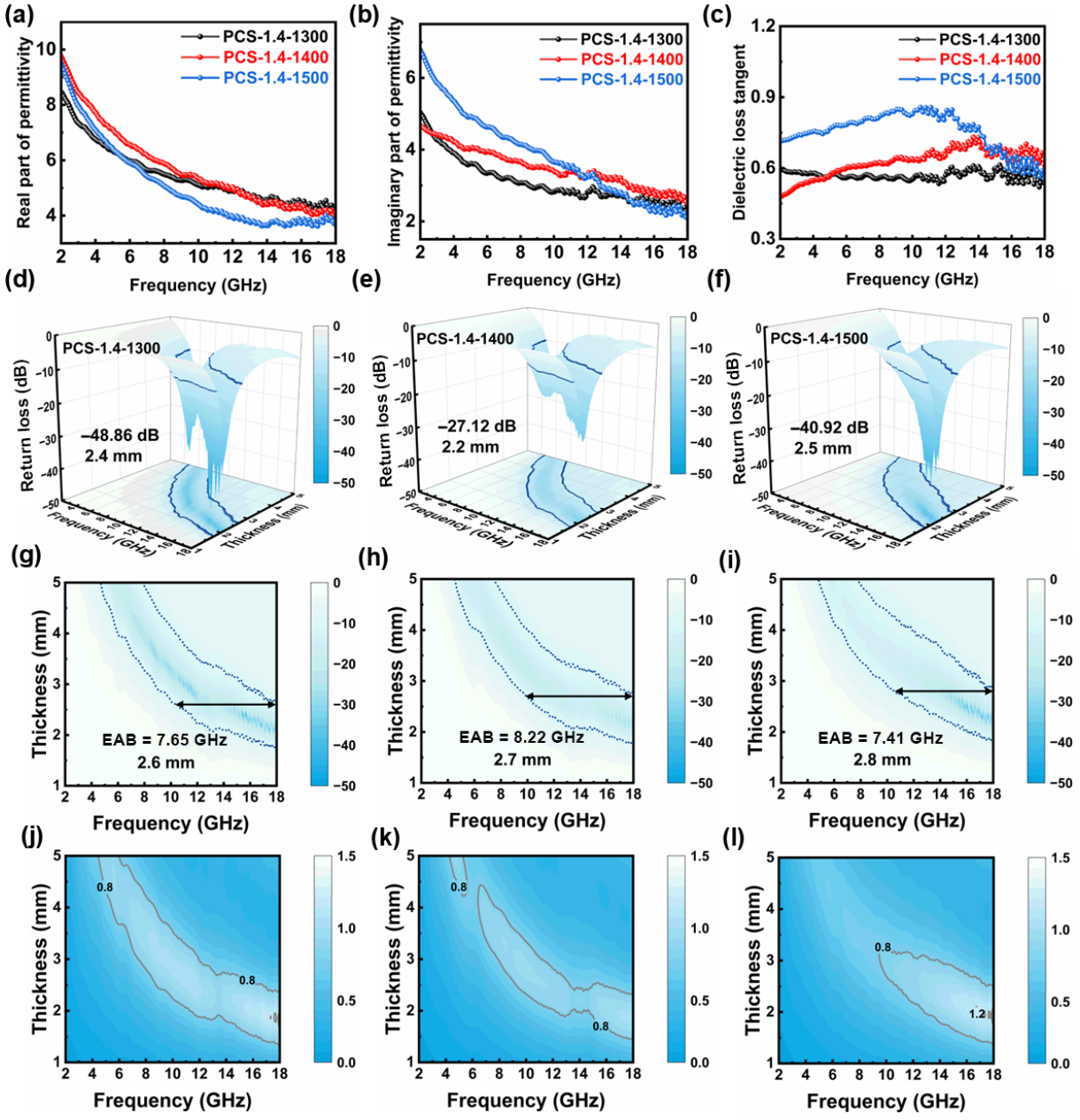

Fig. 4 (a) ε', (b) ε'', (c) $\tan\delta_\varepsilon$ of PCS-1.4-1300, PCS-1.4-1400, PCS-1.4-1500. (d–f) 3D and (g–i) 2D plots of RL for PCS-1.4-1300, PCS-1.4-1400, and PCS-1.4-1500. Normalized impedance maps of (j) PCS-1.4-1300, (k) PCS-1.4-1400, and (l) PCS-1.4-1500.

formation. PCS-1.4-1400 exhibits moderate ε', ε'', and $\tan\delta_\varepsilon$ values, indicating a more balanced dielectric response and optimized attenuation capability.

The dielectric loss results (Fig. S6 in the ESM) reveal that both conduction loss (ε_c'') and polarization loss (ε_p'') increase with pyrolysis temperature, while the proportion of polarization loss rises continuously, reaching its maximum at 1500 °C. Among the three samples, PCS-1.4-1300 achieves the deepest RL_{min} of −48.86 dB, yet its relatively narrow EAB (7.65 GHz) indicates that the absorption is confined to a limited matching frequency range. PCS-1.4-1500 also shows strong attenuation due to enhanced conductive loss, but excessive dielectric loss causes impedance mismatch and restricts the EAB (Fig. 4(l)). In contrast, PCS-1.4-1400 achieves the broadest EAB of 8.22 GHz at 2.7 mm, benefiting from its superior impedance matching over a wider frequency range. The coexistence of nanocrystalline β-SiC, disordered carbon, and amorphous SiO_xC_y in PCS-1.4-1400 provides abundant polarization centers, while the moderately developed conductive network ensures sufficient loss without compromising impedance matching.

Therefore, the sample with a PCS content of 1.4 g pyrolyzed at 1400 °C was identified as the optimal condition for achieving high-performance electromagnetic wave absorption. This result indicates that tailoring the phase composition and graphitization degree of SiC-based fibrous membranes by regulating the PCS content and pyrolysis temperature is a viable strategy for achieving high-efficiency microwave absorption. Furthermore, the microwave absorbing properties of PCS-1.4-1400 are compared with other recently reported SiC-based or SiOC-based ceramic composites, as shown in Fig. 5(d). The PCS-1.4-1400 samples exhibit a clear advantage in achieving a wider EAB at relatively moderate thicknesses [31,53–60].

To evaluate the stealth potential of the optimized PCS-1.4-1400 sample in practical radar applications, the radar cross-section

(RCS) of a perfect electric conductor (PEC) plate, both bare and coated with PCS-1.4-1400 (Fig. 5), was simulated using the Computer Simulation Technology (CST) Studio Suite [61]. The simulation model has dimensions of 100 mm × 100 mm, with a 2.2 mm-thick SiC fiber ceramic absorption layer, and the radar frequency was set at 17.36 GHz. As shown in Fig. 5(a), the as-prepared PCS-1.4-1400 coating exhibits excellent radar stealth properties. Compared with the perfect electric conductor (PEC), a significant RCS reduction is achieved over a wide angular range of −60° to +60°. Notably, the RCS value in the specular reflection direction (0°) decreases from +6.22 to −20.67 dB·m^2, corresponding to a reduction of 26.89 dB, indicating that the scattered power is reduced by approximately 99.8%. The 3D scattering patterns (Figs. 5(b) and 5(c)) further confirm the suppression of the strong scattering lobe and the overall low-scattering characteristics in the entire space. These results demonstrate the promising potential of the obtained sample for wide-angle electromagnetic stealth applications. As shown in Fig. S11 in the ESM, the bistatic scattering RCS pattern of the PCS-1.4-1400 sample exhibits an obvious reduction in scattering intensity over a wide angular range. The average bistatic RCS reaches −13.4 dB·m^2, indicating effective suppression of electromagnetic scattering and promising radar stealth capability.

To better understand distinct scattering behavior, the underlying electromagnetic attenuation mechanisms are schematically illustrated in Fig. 5(e). When electromagnetic waves impinge on electrospun SiC-based fibrous ceramic membranes, the optimized complex permittivity allows more incident waves to penetrate into the interior rather than being directly reflected. The three-dimensional interwoven fibrous architecture prolongs EM wave paths via multiple internal reflections and scattering, thereby enhancing attenuation efficiency compared with bulk counterparts. At the microscopic level, the material consists of crystallized β-SiC, residual free carbon, and amorphous SiO_xC_y phases, forming a heterogeneous multiphase. The abundant interfaces among β-SiC, carbon domains, and amorphous regions act as polarization centers under an alternating electromagnetic field. Charge carriers accumulate at these heterogeneous interfaces, leading to pronounced interfacial polarization. Meanwhile, structural defects and bonding asymmetry within the carbon phase contribute to dipolar polarization [62,63]. These relaxation processes convert electromagnetic energy into thermal energy through dielectric loss [64]. Furthermore, the abundant carbon phases in the sample establish conductive pathways for electron migration and hopping, significantly promoting conduction loss [45]. Meanwhile, the small pores on the fiber surface facilitate additional heat dissipation to the surrounding environment. Together with the continuous three-dimensional

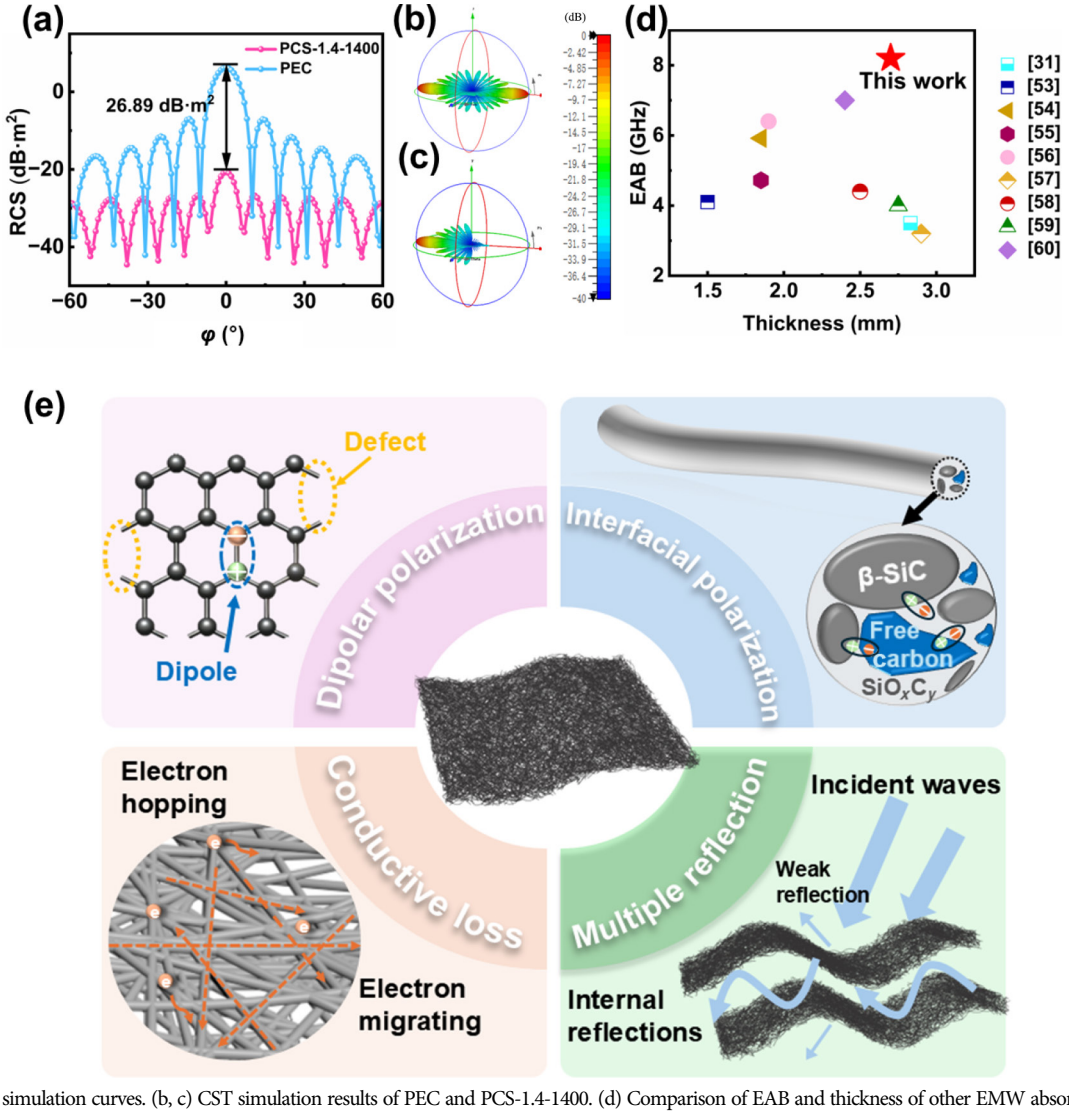

Fig. 5 (a) RCS simulation curves. (b, c) CST simulation results of PEC and PCS-1.4-1400. (d) Comparison of EAB and thickness of other EMW absorbing materials. (e) Schematic illustration of microwave dissipation mechanism of SiC-based fibrous membranes.

清華大学出版社 Tsinghua University Press | SciOpen

fibrous network, these structural features facilitate the efficient transport and dissipation of the converted thermal energy, preventing localized heat accumulation. The synergistic effect of dipolar polarization, interfacial polarization, moderate conduction loss, and multiple internal reflections collectively accounts for the superior microwave absorption performance.

4 Conclusions

In the present work, multiphase SiC-based fibrous ceramic membranes were successfully prepared by combining electrospinning with the PDC route. By regulating the PCS content and pyrolysis temperature, the sample with a PCS content of 1.4 g pyrolyzed at 1400 °C (PCS-1.4-1400) achieves a balanced multiphase structure of β-SiC, SiO_xC_y, and free carbon, which synergistically enhances polarization relaxation, conduction loss, and impedance matching. Consequently, this optimized sample achieves a minimum reflection loss of −27.12 dB at 2.2 mm and a maximum effective absorption bandwidth of 8.22 GHz, covering 9.78–18 GHz, at 2.7 mm. Radar cross-section simulation further confirms its capability to suppress electromagnetic scattering. This study reveals the relationship among precursor composition, phase evolution, dielectric response, and microwave absorption behavior in polymer-derived SiC-based fibrous ceramic membranes, providing guidance for the design of lightweight broadband ceramic absorbers.

Acknowledgements

This work was financially supported by the Henan Province Major Science and Technology Project (No. 261100320100), Zhongyuan Thousand Talents Program - Leading Talents in Science and Technology Innovation (No. 264200510043), the National Natural Science Foundation of China (Nos. 52572086 and 52502079), the Key Research and Development Project of Henan Province (No. 251111232100), the Royal Society Wolfson Visiting Fellowships 2025 Round 1 (No. RSWVF/25/R1/1008), the Natural Science Foundation of Henan (No. 242300421009), and China Postdoctoral Science Foundation (No. 2024M760816).

Author contributions

Gaoang Huang: experiment, data processing, and writing the manuscript. Bingbing Fan and Rui Zhang: experimental design. Wei Li, Limeng Song, and Yu Chen: editing, supervision, review, and revision. Defang Zu, Xuewen Jiang, Mengru Li, Fan Zhang, Hailong Wang, and Yanqiu Zhu: assisting in experiments and reviewing the manuscript.

Availability of data and materials

The data that support the findings of this study are available from the corresponding author upon reasonable request.

Competing interests

The authors have no competing interests to declare that are relevant to the content of this article. The author Bingbing Fan is the Associate Editor of this journal.

Electronic Supplementary Material

Supplementary material is available in the online version of this article at https://doi.org/10.26599/JAC.2026.9221349.

References

[1] Chen ZW, Fan XM, Huang XX, *et al.* Research progress and prospection on high-temperature wave-absorbing ceramic materials. *Adv Ceram* 2020, **41**: 1–98. (in Chinese)

[2] Cai YS, Jia ZR, Wu ZH, *et al.* Selenium nano cluster-modified ZnS/$Co_{1-x}S$@C heterogeneous interface for excellent electromagnetic wave absorption. *J Mater Sci Technol* 2027, **277**: 66–75.

[3] Wang J, Wang YB, Wu JR, *et al.* Synergizing magnetic exchange resonance and hierarchical dielectric relaxation in multiphase core–shell heterojunctions for efficient microwave dissipation. *Acta Phys-Chim Sin* 2026, **42**: 100336.

[4] Song LM, Hu FY, Wang HG, *et al.* Advances in SiC aerogel materials for thermal insulation and electromagnetic wave absorption. *J Adv Ceram* 2026, **15**: 9221316.

[5] Yang Y, Qiao J, Zhang X, *et al.* Electrospun magnetic carbon nanofibers for electromagnetic wave absorption: A review. *J Mater Sci Technol* 2026, **265**: 1–22.

[6] Shao GF, Xu RP, Chen Y, *et al.* Miniaturized hard carbon nanofiber aerogels: From multiscale electromagnetic response manipulation to integrated multifunctional absorbers. *Adv Funct Mater* 2024, **34**: 2408252.

[7] Peng HL, Cai B, Zhang Y, *et al.* Radar-terahertz-infrared compatible stealth coaxial silver nanowire@carbon nano-cable aerogel. *Angew Chem Int Edit* 2025, **64**: 202421090.

[8] Fu ZY, Pang AM, Luo H, *et al.* Research progress of ceramic matrix composites for high temperature stealth technology based on multi-scale collaborative design. *J Mater Res Technol* 2022, **18**: 2770–2783.

[9] Liu JL, Zhang LM, Wu HJ. Electromagnetic wave-absorbing performance of carbons, carbides, oxides, ferrites and sulfides: Review and perspective. *J Phys D Appl Phys* 2021, **54**: 203001.

[10] Chen JH, Liu M, Yang T, *et al.* Improved microwave absorption performance of modified SiC in the 2–18 GHz frequency range. *CrystEngComm* 2017, **19**: 519–527.

[11] Kuang JL, Xiao T, Hou XJ, *et al.* Microwave synthesis of worm-like SiC nanowires for thin electromagnetic wave absorbing materials. *Ceram Int* 2019, **45**: 11660–11667.

[12] Zhao HQ, Liao QW, Li YH, *et al.* Additive manufacturing of silicon carbide microwave-absorbing metamaterials. *Addit Manuf Front* 2025, **4**: 200186.

[13] Abdalla I, Cai JY, Lu W, *et al.* Recent progress on electromagnetic wave absorption materials enabled by electrospun carbon nanofibers. *Carbon* 2023, **213**: 118300.

[14] Zhang SB, Liao CJ, Wang XY, *et al.* Effects of SiBCN modification on the mechanical and electromagnetic wave absorption properties of SiC_f/SiC composites. *Ceram Int* 2026, **52**: 11109–11118.

[15] Wang XZ, Zhao WX, Liu MY. Effect of sintering atmosphere on properties of near stoichiometric silicon carbide fibers. *J Am Ceram Soc* 2026, **109**: 70277.

[16] Wang XG, Shi GM, Shi FN, *et al.* Facile synthesis and tunable microwave absorption properties of N-doped C modified SiC nanoparticles. *J Mater Sci—Mater El* 2023, **34**: 1072.

[17] Feng P, Wei HJ, Shang P, *et al.* Enhanced electromagnetic microwave absorption of SiC nanowire-reinforced PDC–SiC ceramics catalysed by rare earth. *Ceram Int* 2022, **48**: 24915–24924.

[18] Qi Q, Li T, Yang H, *et al.* Recent advances in structural engineering of ceramic microwave absorption materials: From nano/micro architectures to macroscale design. *J Adv Ceram* 2025, **14**: 9221205.

[19] Xu JJ, Wang L, Wang XM, *et al.* Research progress of high temperature absorbing materials. *Adv Ceram* 2024, **3**: 189–205. (in Chinese)

[20] Guo RD, Su D, Chen F, *et al.* Hollow beaded Fe_3C/N-doped carbon fibers toward broadband microwave absorption. *ACS Appl Mater Inter* 2022, **14**: 3084–3094.

[21] Zhao YJ, Zhang YN, Yang CR, *et al.* Ultralight and flexible SiC nanoparticle-decorated carbon nanofiber mats for broad-band microwave absorption. *Carbon* 2021, **171**: 474–483.

[22] Huang XG, Cong WJ, Chen Y, *et al.* Conductive network reconstruction driven by carbonization: Enabling the transition of hard carbon from electromagnetic wave absorption to shielding. *Carbon* 2026, **251**: 121326.

[23] Yu GY, Shao GF, Xu ZL, *et al.* Hierarchical interface-engineered

magnetic graphene–SiCN aerogels via a stepwise confinement strategy for low-frequency and broadband microwave absorption. *J Adv Ceram* 2025, **14**: 9221187.
[24] Tang HQ, Ren K, Wang YG. Polysiloxane encapsulating strategy to enhance the high-temperature electromagnetic wave absorption performance of carbon-rich SiOC ceramics. *Ceram Int* 2024, **50**: 51392–51402.
[25] Qian JJ, Ma DD, Zou YX, *et al.* Implanting Ag nanoparticles in SiOC ceramic nanospheres for exceptional electromagnetic wave absorption and antibacterial performance. *J Adv Ceram* 2025, **14**: 9221084.
[26] Xue JM, Tang ZM, Wang CX, *et al.* Microstructure and EMW absorption properties of PDCs–SiCN(Ti) ceramics with adjustable SiC nanowires and TiC nanocrystallines. *Mater Res Bull* 2024, **176**: 112804.
[27] Jia YJ, Ajayi TD, Roberts MA Jr, *et al.* Ultrahigh-temperature ceramic–polymer-derived SiOC ceramic composites for high-performance electromagnetic interference shielding. *ACS Appl Mater Inter* 2020, **12**: 46254–46266.
[28] Yang YJ, Dong YP, Liu YY, *et al.* Research progress of wave-absorbing SiCN ceramics. *Adv Ceram* 2025, **46**: 360–376. (in Chinese)
[29] Yu GY, Shao GF, Xu RP, *et al.* Metal-organic framework-manipulated dielectric genes inside silicon carbonitride toward tunable electromagnetic wave absorption. *Small* 2023, **19**: 2304694.
[30] Feng YR, Guo X, Huang K, *et al.* Enhanced electromagnetic microwave absorption of SiOC ceramics targeting the integration of structure and function. *J Eur Ceram Soc* 2021, **41**: 6393–6405.
[31] Duan WY, Yin XW, Ye F, *et al.* Synthesis and EMW absorbing properties of nano SiC modified PDC–SiOC. *J Mater Chem C* 2016, **4**: 5962–5969.
[32] Wu F, Qiang SY, Zhang XH, *et al.* The rising of flexible and elastic ceramic fiber materials: Fundamental concept, design principle, and toughening mechanism. *Adv Funct Mater* 2022, **32**: 2207130.
[33] Sharma GK, James NR. Progress in electrospun polymer composite fibers for microwave absorption and electromagnetic interference shielding. *ACS Appl Electron Ma* 2021, **3**: 4657–4680.
[34] Bhardwaj N, Kundu SC. Electrospinning: A fascinating fiber fabrication technique. *Biotechnol Adv* 2010, **28**: 325–347.
[35] Wang P, Cheng LF, Zhang YN, *et al.* Flexible, hydrophobic SiC ceramic nanofibers used as high frequency electromagnetic wave absorbers. *Ceram Int* 2017, **43**: 7424–7435.
[36] Chen QQ, Li DX, Liao XQ, *et al.* Polymer-derived lightweight SiBCN ceramic nanofibers with high microwave absorption performance. *ACS Appl Mater Inter* 2021, **13**: 34889–34898.
[37] Chai YX, Zhang HY, Zhou XG, *et al.* Effect of pyrolysis temperatures on the performance of SiC_f/SiC composites. *Fusion Eng Des* 2017, **125**: 447–453.
[38] Zimbone M, Barbagiovanni EG, Bongiorno C, *et al.* Generation and termination of stacking faults by inverted domain boundaries in 3C-SiC. *Cryst Growth Des* 2020, **20**: 3104–3111.
[39] Pujar VV, Cawley JD. Effect of stacking faults on the X-ray diffraction profiles of β-SiC powders. *J Am Ceram Soc* 1995, **78**: 774–782.
[40] Huang LY, Wang H, Ouyang Q, *et al.* Highly crystalline SiC fibers with enhanced microwave absorption properties via boron doping and electron beam irradiation oxidation curing. *Ceram Int* 2025, **51**: 21235–21245.
[41] Wang P, Cheng LF, Zhang YN, *et al.* Electrospinning of graphite/SiC hybrid nanowires with tunable dielectric and microwave absorption characteristics. *Compos Part A—Appl S* 2018, **104**: 68–80.
[42] Ouyang Q, Wang YF, Huang J, *et al.* TG-MS analysis on the degradation behavior and mechanism of amorphous SiC_xO_y phase in polyaluminocarbosilane-derived Si–Al–C–O fiber. *J Therm Anal Calorim* 2022, **147**: 11759–11767.
[43] Wang JL, Li YF, Cao JR, *et al.* Robust and thermally insulating SiBCN/SiOC ceramic aerogel with superior electromagnetic wave absorption performance and high-temperature stability up to 1600 °C. *J Adv Ceram* 2026, **15**: 9221256.
[44] An ZM, Ye CS, Zhang RB, *et al.* Flexible and recoverable SiC nanofiber aerogels for electromagnetic wave absorption. *Ceram Int* 2019, **45**: 22793–22801.
[45] Wang P, Cheng LF, Zhang YN, *et al.* Synthesis of SiC nanofibers with superior electromagnetic wave absorption performance by electrospinning. *J Alloy Compd* 2017, **716**: 306–320.
[46] Zhang S, Niu RF, Guo XM, *et al.* Designing multiscale integration of hierarchical gradient heterostructures for enhanced electromagnetic protection performance. *Carbon* 2026, **252**: 121371.
[47] Li MR, Li W, Wang YX, *et al.* Entropy-driven microwave absorption enhancement in hexagonal $(Ba_{1/3}Sr_{1/3}Ca_{1/3})FeO_3$ perovskite. *J Adv Ceram* 2025, **14**: 9221059.
[48] Wang CG, Chen PG, Li XC, *et al.* Enhanced electromagnetic wave absorption for Y_2O_3-doped SiBCN ceramics. *ACS Appl Mater Inter* 2021, **13**: 55440–55453.
[49] Wu GR, Zhu JH, Guo XM, *et al.* Construction of Schottky barrier and the enhanced interface polarization effect of C@ZnO/Sn@GaN for high performance electromagnetic wave absorption. *Acta Phys-Chim Sin* 2026, **42**: 100324.
[50] Duan WY, Yin XW, Li Q, *et al.* Synthesis and microwave absorption properties of SiC nanowires reinforced SiOC ceramic. *J Eur Ceram Soc* 2014, **34**: 257–266.
[51] Zhang YN, Zhao YJ, Chen Q, *et al.* Flexible SiC–CNTs hybrid fiber mats for tunable and broadband microwave absorption. *Ceram Int* 2021, **47**: 8123–8132.
[52] Jia ZR, Zhou ZH, Xu S, *et al.* Two birds with one stone: Phosphorus doping to enhance conduction loss and dipole polarization for electromagnetic wave absorber. *Acta Phys-Chim Sin* 2026, **42**: 100310.
[53] Huo YS, Zhao K, Xu ZL, *et al.* Electrospinning synthesis of SiC/Carbon hybrid nanofibers with satisfactory electromagnetic wave absorption performance. *J Alloy Compd* 2020, **815**: 152458.
[54] Pang L, Xiao P, Li Z, *et al.* Long-range uniform SiC_xO_y beaded carbon fibers for efficient microwave absorption. *ACS Appl Mater Inter* 2023, **15**: 30815–30825.
[55] Zhang MY, Miao P, Zhang HN, *et al.* High efficiency microwave absorption and infrared suppression synergistic strategy for 3D Fe_3C /C–SiCN fibers via electrospinning. *Chem Eng J* 2026, **529**: 173200.
[56] Wang P, Cheng LF, Zhang YN, *et al.* Flexible SiC/Si_3N_4 composite nanofibers with *in situ* embedded graphite for highly efficient electromagnetic wave absorption. *ACS Appl Mater Inter* 2017, **9**: 28844–28858.
[57] Wei HJ, Zhou CL, Feng P, *et al.* Rear earth (Re: Sc, Y, and Ce) modified PDCs–SiC ceramics for efficient microwave absorption. *Mater Charact* 2022, **190**: 112048.
[58] Wu XH, Zhang XS, Zhang SH, *et al.* Microwave absorption properties of CNT/SiC micro/nanofibers. *J Ceram* 2025, **46**: 580–587. (in Chinese)
[59] Xue JM, Liu XL, Wang YQ, *et al.* *In situ* growth of SiCnws in $Sc(NO_3)_3$ modified polysiloxane-derived SiOC ceramics for enhanced microwave absorbing performance. *J Am Ceram Soc* 2025, **108**: 70087.
[60] Chen YT, Peng HL, Cai B, *et al.* Synthesis of ultralight hollow SiC/C nanofiber for highly efficient electromagnetic wave absorption. *J Adv Ceram* 2026, **15**: 9221225.
[61] Lv FY, Wang YQ, He QC, *et al.* High-entropy strategy-driven lattice distortion and electronic rearrangement in MOF-derived HEA/NC composites for balanced electromagnetic response and superior microwave attenuation. *Adv Funct Mater* 2026, **36**: 75416.
[62] Zhang MH, Chang M, Tian WT, *et al.* Interfacial modulation of SiC/TiC hybrid nanofibers for fabricating flexible ceramic electromagnetic wave absorbers. *Mater Res Bull* 2024, **178**: 112883.
[63] Duan YP, Liu J, Zhang YH, *et al.* First-principles calculations of graphene-based polyaniline nano-hybrids for insight of electromagnetic properties and electronic structures. *RSC Adv* 2016, **6**: 73915–73923.
[64] Xu S, Jia ZR, Lan D, *et al.* Synergistic polarization relaxation in multi-level hybridization and preferred orientation strategies for electromagnetic wave absorption. *Adv Funct Mater* 2026, **36**: 75567.